

Article

# Effect of $Zr^{4+}$ on Lithium-Ion Conductivity of Garnet-Type $Li_{5+x}La_3(Nb_{2-x}Zr_x)O_{12}$ Solid Electrolytes

Shirley Reis <sup>1,\*</sup>, Robson Grosso <sup>1</sup>, Juliane Kosctiuk <sup>1</sup>, Marianne Franchetti <sup>1</sup>, Francisca Oliveira <sup>1</sup>, Adler Souza <sup>1</sup>, Cyrille Gonin <sup>1</sup>, Heverson Freitas <sup>1</sup>, Robson Monteiro <sup>2</sup>, Luanna Parreira <sup>2</sup> and Marcos Berton <sup>1</sup>

<sup>1</sup> SENAI Institute for Innovation in Electrochemistry, Curitiba 80215-090, PR, Brazil

<sup>2</sup> Companhia Brasileira de Metalurgia e Mineração (CBMM), Araxá 38183-903, MG, Brazil

\* Correspondence: shirley.reis@sistemafiep.org.br

**Abstract:** Garnet-type structured electrolytes are considered a key technology for the next generation of lithium-ion batteries such as all-solid-state batteries. Cubic Garnet-type solid oxides with composition  $Li_{5+x}La_3(Nb_{2-x}Zr_x)O_{12}$  ( $x$  between 0 and 1.5) were synthesized by solid-state reaction and sintered by spark plasma sintering. Powder characterization indicates the formation of solid solution with high chemical homogeneity and spherical particles. High relative densities (>96%) were obtained by spark plasma sintering at 950 °C for 10 min and pressure application of 50 MPa. Although the formation of secondary phase  $La_2Zr_2O_7$  was identified by the X-ray diffraction patterns of Zr-doped pellets, it has been eliminated for  $x = 0.75$  and 1 by conventional heat treatment at 850 °C for 1 h. High ionic conductivity values were attained for  $x \geq 0.75$ , reaching a maximum value in the order of  $10^{-4}$  S.cm<sup>-1</sup> at 25 °C with activation energy of 0.38 eV. The results indicated that  $Zr^{4+}$  promoted significant increasing of the lithium-ion conductivity by lowering the activation energy.

**Keywords:** garnet-type oxides; solid electrolytes; spark plasma sintering; ceramics; lithium-ion conductivity



**Citation:** Reis, S.; Grosso, R.; Kosctiuk, J.; Franchetti, M.; Oliveira, F.; Souza, A.; Gonin, C.; Freitas, H.; Monteiro, R.; Parreira, L.; et al. Effect of  $Zr^{4+}$  on Lithium-Ion Conductivity of Garnet-Type  $Li_{5+x}La_3(Nb_{2-x}Zr_x)O_{12}$  Solid Electrolytes. *Batteries* **2023**, *9*, 137. <https://doi.org/10.3390/batteries9020137>

Academic Editors: Irina A. Stenina and Chunwen Sun

Received: 18 November 2022

Revised: 10 January 2023

Accepted: 16 January 2023

Published: 15 February 2023



**Copyright:** © 2023 by the authors. Licensee MDPI, Basel, Switzerland. This article is an open access article distributed under the terms and conditions of the Creative Commons Attribution (CC BY) license (<https://creativecommons.org/licenses/by/4.0/>).

## 1. Introduction

Nowadays, lithium-ion batteries (LIBs) are widely employed in many electronic devices and have assisted in the development and evolution of technology by powering portable electronics [1,2]. Due to the growth of interest in electric vehicles and increasing concern regarding sustainability and clean energy, it has been predicted that the LIBs market will need to undergo a huge expansion to fulfill the demand for rechargeable batteries [3]. However, there are many roadblocks that may hinder this development, among them the safety hazard issue that arises due to the possibility of battery thermal runaway and subsequent leakages and explosions during their usage [4,5]. These shortcomings happen because of the highly flammable organic liquid electrolytes present in the batteries and the hazardous compounds formed by their degradation [6,7]. To address this issue, the substitution of the liquid electrolyte by solid compounds to create the all-solid-state battery (ASSB) has been an interesting approach that leads LIB technology to the next level. Thus, the interest for solid electrolytes has emerged as an alternative since they are not flammable, show high thermal and electrochemical stability, high energy density, and mechanical stability, even after being submitted to stress such as cutting and bending [8,9].

Cubic Garnet-type structured materials [10] are considered promising candidates for solid electrolyte applications in ASSB. Among the most studied Garnet oxides are  $Li_5La_3Nb_2O_{12}$  (LLN) [11–14] and  $Li_7La_3Zr_2O_{12}$  (LLZ) [14,15]. Different amounts of Li in the compounds are due to the balance of charge caused by the oxidation state of cations located at octahedrons sites (i.e.,  $Nb^{5+}$  and  $Zr^{4+}$ ) [16]. The lithium-ion conductivity of these materials was reported to be in the order of  $10^{-5}$ – $10^{-7}$  S.cm<sup>-1</sup> for LLN [11–14,17–21] and  $10^{-4}$  S.cm<sup>-1</sup> for LLZ at 25 °C [14,15,22]. As an attempt to increase ionic conductivity and avoid tetragonal phase formation for LLZ, the substitution of atoms has been

investigated. In this sense, it has been demonstrated that LLZ-doped compounds with formula  $\text{Li}_{7-x}\text{La}_3(\text{Zr}_{2-x}\text{M}_x)\text{O}_{12}$  ( $\text{M} = \text{Nb}^{5+}, \text{Ta}^{5+}$ ) show an increase of one order of magnitude depending on the cation dopants and concentration with activation energy within the range of 0.3–0.4 eV [10,14,22–24]. In addition, a similar effect was observed for  $\text{Li}_{5+x}\text{La}_3(\text{Nb}_{2-x}\text{Ce}_x)\text{O}_{12}$  solid solutions for  $x = 0.75$  with long-term cycling stability over 380 h at 55 °C [13]. The highest total conductivity of  $1.38 \times 10^{-4} \text{ S.cm}^{-1}$  reported for  $\text{Li}_{5+2x}\text{La}_3\text{Nb}_{2-x}\text{Sc}_x\text{O}_{12}$  was observed for  $x = 0.625$  at 25 °C [25], while  $\text{Li}_{5+2x}\text{La}_3\text{Nb}_{2-x}\text{Pr}_x\text{O}_{12}$  shows a value of  $4.1 \times 10^{-4} \text{ S.cm}^{-1}$  at 21 °C [26]. In order to compare data from the literature, total ionic conductivity values obtained at 25 °C and activation energy reported for undoped and doped LLN and LLZ Garnet-type ceramics are listed in Table 1.

**Table 1.** Literature-reported data of the total ionic conductivity ( $\sigma_{25^\circ\text{C}}$ ), activation energy ( $E_a$ ), and relative density ( $\rho_R$ ) of LLN and LLZ-based Garnet-structured solid electrolytes sintered by conventional sintering (CS) and spark plasma sintering (SPS).

| Formula  | $x$   | Sintering | $\rho_R$ (%) | $\sigma_{25^\circ\text{C}}$ ( $\text{S.cm}^{-1}$ ) | $E_a$ (eV) | Ref. |
|--|-------|-----------|--------------|--|------------|------|
| LLN  |       |           |              |  |            |      |
| $\text{Li}_5\text{La}_3\text{Nb}_2\text{O}_{12}$                       | -     | CS        | 93.7         | $2.5 \times 10^{-5}$                               | -          | [17] |
| $\text{Li}_5\text{La}_3\text{Nb}_2\text{O}_{12}$                       | -     | CS        | -            | $8.0 \times 10^{-6}$                               | 0.43       | [18] |
| $\text{Li}_5\text{La}_3\text{Nb}_2\text{O}_{12}$                       | -     | CS        | -            | $2.54 \times 10^{-7}$                              | 0.51       | [19] |
| $\text{Li}_5\text{La}_3\text{Nb}_2\text{O}_{12}$                       | -     | CS        | 89–92        | $3.73 \times 10^{-5}$                              | 0.43       | [14] |
| $\text{Li}_5\text{La}_3\text{Nb}_2\text{O}_{12}$                       | -     | SPS       | 89           | $2.7 \times 10^{-6}$                               | -          | [20] |
| $\text{Li}_5\text{La}_3\text{Nb}_2\text{O}_{12}$                       | -     | SPS       | -            | $6.99 \times 10^{-6}$                              | 0.59       | [21] |
| LLZ  |       |           |              |  |            |      |
| $\text{Li}_7\text{La}_3\text{Zr}_2\text{O}_{12}$                       | -     | CS        | -            | $7.74 \times 10^{-4}$                              | -          | [15] |
| $\text{Li}_7\text{La}_3\text{Zr}_2\text{O}_{12}$                       | -     | CS        | -            | $1.68 \times 10^{-4}$                              | 0.36       | [22] |
| $\text{Li}_7\text{La}_3\text{Zr}_2\text{O}_{12}$                       | -     | CS        | 89–92        | $3.01 \times 10^{-4}$                              | 0.33       | [14] |
| Doped LLZ  |       |           |              |  |            |      |
| $\text{Li}_{7-x}\text{La}_3(\text{Zr}_{2-x}\text{Nb}_x)\text{O}_{12}$  | 0.25  | CS        | 89–92        | $8.19 \times 10^{-4}$                              | 0.30       | [14] |
| $\text{Li}_{7-x}\text{La}_3(\text{Zr}_{2-x}\text{Nb}_x)\text{O}_{12}$  | 0.5   | CS        | 89–92        | $3.74 \times 10^{-4}$                              | 0.32       | [14] |
| $\text{Li}_{7-x}\text{La}_3(\text{Zr}_{2-x}\text{Nb}_x)\text{O}_{12}$  | 0.4   | CS        | 87.3         | $5.09 \times 10^{-4}$                              | 0.31       | [23] |
| $\text{Li}_{7-x}\text{La}_3(\text{Zr}_{2-x}\text{Ta}_x)\text{O}_{12}$  | 0.5   | CS        | -            | $5.22 \times 10^{-4}$                              | 0.32       | [22] |
| $\text{Li}_{7-x}\text{La}_3(\text{Zr}_{2-x}\text{Ta}_x)\text{O}_{12}$  | 0.56  | SPS       | -            | $1.35 \times 10^{-3}$                              | 0.41       | [22] |
| $\text{Li}_{7-x}\text{La}_3(\text{Zr}_{2-x}\text{Ta}_x)\text{O}_{12}$  | 0.5   | SPS       | 95.5         | $6.9 \times 10^{-4}$                               | 0.42       | [24] |
| Doped LLN  |       |           |              |  |            |      |
| $\text{Li}_{5+x}\text{La}_3(\text{Nb}_{2-x}\text{Ce}_x)\text{O}_{12}$  | 0.75  | CS        | 75.1         | $1.4 \times 10^{-4}$                               | 0.35       | [13] |
| $\text{Li}_{5+x}\text{La}_3(\text{Nb}_{2-x}\text{Ge}_x)\text{O}_{12}$  | 0.75  | CS        | 92.0         | $1.2 \times 10^{-4}$                               | -          | [27] |
| $\text{Li}_{5+x}\text{La}_3(\text{Nb}_{2-x}\text{Hf}_x)\text{O}_{12}$  | 1     | CS        | -            | $5.0 \times 10^{-5}$                               | -          | [28] |
| $\text{Li}_{5+2x}\text{La}_3(\text{Nb}_{2-x}\text{Sc}_x)\text{O}_{12}$ | 0.625 | CS        | 92–95        | $1.38 \times 10^{-4}$                              | 0.36       | [25] |
| $\text{Li}_{5+2x}\text{La}_3(\text{Nb}_{2-x}\text{Sm}_x)\text{O}_{12}$ | 0.30  | CS        | 78           | $5.84 \times 10^{-5}$                              | 0.38       | [29] |
| $\text{Li}_5\text{La}_3(\text{Nb}_{2-x}\text{V}_x)\text{O}_{12}$       | 0.15  | CS        | -            | $6.0 \times 10^{-6}$                               | 0.37       | [30] |
| $\text{Li}_{5+2x}\text{La}_3(\text{Nb}_{2-x}\text{Y}_x)\text{O}_{12}$  | 0.75  | CS        | -            | $2.99 \times 10^{-4}$                              | 0.42       | [31] |

Several synthesis methods have been applied to produce cubic Garnet solid solutions, including coprecipitation [32], sol-gel [12], spray pyrolysis [20], and solid-state reaction [15], among others. Although wet chemical synthesis might allow lowering sintering temperature and dwell time due to particle size decreasing, conventional sintering (CS) conditions which are required to obtain dense pellets might be a detrimental factor to phase stability mainly due to the loss of Li [24]. The Spark Plasma Sintering (SPS) technique allows application of low temperatures (<1000 °C) and short dwell times (<10 min) compared to a conventional process due to the simultaneous application of temperature and uniaxial pressure [33]. As examples of solid electrolytes sintered by SPS, lithium-ion conductivity of  $6.9 \times 10^{-4} \text{ S.cm}^{-1}$  at 25 °C and critical current density of  $200 \text{ mA.cm}^{-2}$  for short-circuit was reported for  $\text{Li}_{6.5}\text{La}_3(\text{Zr}_{1.5}\text{Ta}_{0.5})\text{O}_{12}$  sintered at 1000 °C for 10 min at

37.5 MPa [24], highly dense pellets (99.8%) of  $\text{Li}_{6.87}\text{La}_{2.97}(\text{Zr}_{1.60}\text{Ta}_{0.56})\text{O}_{12}$  with conductivity of  $1.35 \times 10^{-3} \text{ S}\cdot\text{cm}^{-1}$  and activation energy of 0.41 eV were obtained at 1000 °C for 10 min [22], and LLN dense pellets (89%) were produced at 950 °C for 30 min [20]. Therefore, it is evident that the combination of cation substitution and use of SPS to produce dense ceramics might improve the ionic conductivity of Garnet-type solid solutions.

Although  $\text{Ta}^{5+}$  promoted the highest ionic conductivity in doped LLZ solid solutions [22,24], several other elements show promise for application as dopants in solid electrolytes in ASSB. Garnet-type structured LLN doped with  $\text{Y}^{3+}$  and  $\text{Sc}^{3+}$ , for example, have shown good ionic conductivity in the order of  $10^{-4} \text{ S}\cdot\text{cm}^{-1}$  [25,31] despite the low ionic conductivity of undoped LLN. The data reported in the current literature indicate that more investigations need to be conducted as an attempt to identify a new composition range with higher ionic conductivity values.

Thus, in aiming for improvement of the lithium-ion conductivity of LLN-based solid electrolytes, in the current work, we have investigated an underexplored range of solid solutions of  $\text{Li}_{5+x}\text{La}_3(\text{Nb}_{2-x}\text{Zr}_x)\text{O}_{12}$  ( $0 \leq x \leq 1.5$ ) synthesized by solid-state reaction and sintered by the SPS method, which allows the production of highly dense pellets in short sintering dwell times.

## 2. Materials and Methods

$\text{Li}_{5+x}\text{La}_3(\text{Nb}_{2-x}\text{Zr}_x)\text{O}_{12}$  (LLNZ, SENAI, Curitiba, PR, Brazil) solid solutions, where  $x$  ranged between 0 and 1.5, were produced by solid-state reaction synthesis. Stoichiometric amounts of  $\text{Li}_2\text{CO}_3$  (Sigma-Aldrich, St. Louis, MO, USA),  $\text{La}_2\text{O}_3$  (Sigma-Aldrich, St. Louis, MO, USA),  $\text{Nb}_2\text{O}_5$  (CBMM, Araxá, MG, Brazil), and  $\text{ZrO}_2$  (Sigma-Aldrich, St. Louis, MO, USA) were wet ball milled in a planetary ball mill machine (Retsch, PM 100) using 10 mm diameter zirconia spheres in isopropyl alcohol. Sequential milling/calcination steps were used. The first milling was conducted at 350 rpm for 12 h followed by two-step continuous heat treatment at 400 °C for 1 h and 800 °C for 12 h. The second milling was conducted at 400 rpm for 6 h, then powders were calcined at 800 °C for 12 h. Finally, LLNZ solid solutions were milled at 100 rpm for 10 min to minimize powder agglomeration [20]. Flowcharts of the methodology performed in this work are presented in Figure 1. Each step of the solid-state reaction synthesis is represented in the schematic diagram in Figure 1a. An illustration of the cubic Garnet-type structure is also shown in Figure 1a, where the blue dodecahedra and the green octahedra represent sites occupied by  $\text{La}^{3+}$  and  $\text{Nb}^{5+}/\text{Zr}^{4+}$ , respectively. Red spheres represent  $\text{O}^{2-}$  ions, with pink and white spheres representing  $\text{Li}^+$  ions within the Garnet structure. The crystal structure was drawn with VESTA software [34] using ICSD #171171 [35].

Densification of the pellets was accomplished by SPS (GT Advanced Technologies Inc., SPS 10-4). The typical procedure was performed by loading the synthesized powders into a 10 mm diameter graphite die lined with graphite sheets. The assembly was placed into a vacuum chamber and heated to 450 °C with simultaneous application of pressure. Temperature was held constant for 10 min to ensure thermal equilibrium was reached throughout the sample and was then increased to 950 °C by applying a heating rate of  $50 \text{ }^\circ\text{C}\cdot\text{min}^{-1}$ . Pressure was continuously increased to reach the maximum value of 50 MPa, which was released after the dwell time of 10 min. A cooling rate of  $200 \text{ }^\circ\text{C}\cdot\text{min}^{-1}$  was applied. A representative diagram of temperature and pressure profiles is shown in Figure 1b. Dense pellets with 2 mm thickness were produced by this sintering process. Samples were heat treated at 850 °C for 1 h in order to eliminate residual carbon from the surface of the samples and then stored in an argon-filled glovebox (MBraun, UNILab Pro SP). The relative density of sintered pellets was measured by the Archimedes method and compared to the theoretical density obtained by the Rietveld refinement of the samples. X-ray diffraction (XRD) was performed in a diffractometer (Bruker, D2 Phaser) with Bragg–Brentano configuration using  $\text{Cu K}\alpha$  radiation and a Ni filter. Powder and sintered pellets were measured in the 10–75° angular range with 0.02° step size and 2 s counting time. Rietveld refinement was performed using TOPAS software. Microstructural characterization of the synthesized

powders was performed by scanning electron microscopy (SEM, Hitachi, TM3000) coupled with energy-dispersive X-ray spectroscopy (EDS, Bruker, Quantax 70). Images of the dense pellets were also obtained by SEM after heat treatment, allowing microstructural evaluation and determination of the average grain size by measuring at least 500 grains per sample. For impedance measurements, Au electrode layers were deposited on both sides of the pellets by the physical vapor deposition (PVD) technique (MBraun, EcoVap 5G). Samples were placed in a Swagelok-type cell and sealed. Both electrode deposition and sample assembly were performed under argon into the glovebox to avoid undesired reactions on the sample surface, which might occur during moisture and CO<sub>2</sub> exposure. The conductivity was determined by an impedance spectroscopy analyzer (Solartron, SI 1260) within the frequency range of 1 kHz to 13 MHz with an amplitude of 10 mV. Measurements were performed as a function of temperature from 25 to 70 °C by using a homemade 100 mL volume tube furnace. This furnace is made of a silicone rubber heating element rolled in a glass tube, which is wrapped by a ceramic tube.

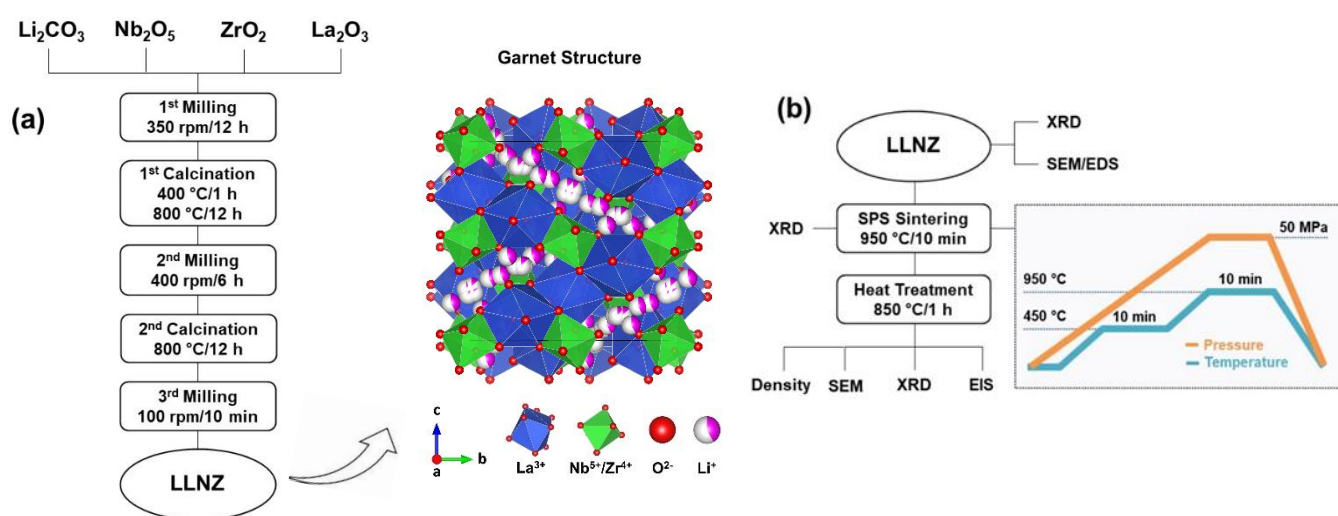


**Figure 1.** Flowcharts of the (a) solid–state reaction synthesis of the LLNZ powders with a representation of the Garnet–type structure and (b) characterization techniques used for powders and dense pellets with the spark plasma sintering profile.

### 3. Results and Discussion

LLNZ powders were successfully synthesized by solid-state reaction as evidenced by physical–chemical characterization. XRD patterns of the LLNZ powders with different Zr contents ( $x$ ) are shown in Figure 2. Cubic Garnet-type structure (ICSD #171171) [35] was indexed for all diffraction peaks for each produced powder. The narrow and sharp peaks indicate good crystallinity of the materials, while the agreement between the experimental XRD results and adjusted profiles achieved by the refinement of the lattice parameters through the Rietveld method confirms that the material shows a predominantly Garnet-type crystal structure with less than 0.5% of pyrochlore phase, especially for  $x = 0.75$ , 1, and 1.5. As an example, refinement of the LLNZ with  $x = 0.75$  (represented by LLNZ0.75) is exhibited in Figure 3, with  $R_{wp}$  and  $R_p$  weighted profile  $R$ -factors listed in Table 2. Rietveld refinements indicated that LLNZ with different Zr content are composed by Garnet structure with space group  $Ia-3d$  [13,35]. A small amount (<1%) of the secondary phase of  $\text{La}_2\text{Zr}_2\text{O}_7$  was detected only in the composition of  $x = 0.25$  (LLNZ0.25), as indicated in Figure 2. Less than 0.5% of the secondary phase  $\text{LiLa}_2\text{NbO}_6$  was detected for samples where  $x = 0.75$ , 1, and 1.5, also shown in Figure 2. The evolution of the lattice parameter as a function of  $x$  is presented in Figure 4. The lattice parameter of 12.8362 Å for undoped ( $x = 0$ , i.e., LLNZ0) material is within the range of values previously reported for  $\text{Li}_5\text{La}_3\text{Nb}_2\text{O}_{12}$  [11]. The observed linear increasing indicates that  $\text{Nb}^{5+}$  (0.64 Å) [36] has been replaced by  $\text{Zr}^{4+}$  ions (0.72 Å) [36] resulting in solid solution formation, which

is expected according to Vegard's law [26] and agrees with reports in the literature for Nb-doped LLZ compositions [14]. The refined lattice parameter and theoretical density values are reported in Table 2.

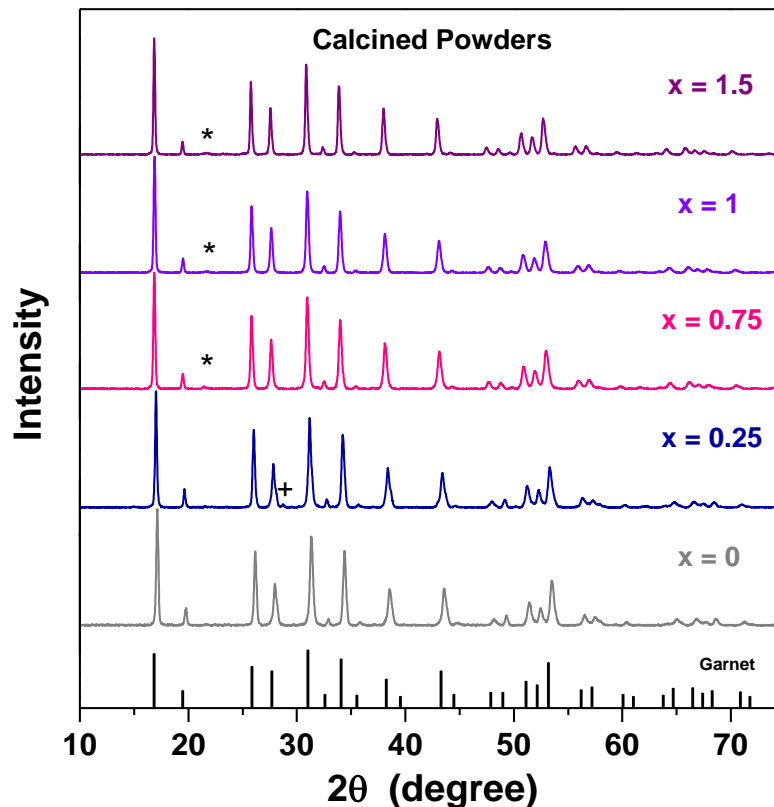


Figure 2. XRD patterns of LLNZ calcined powders. (+)  $\text{La}_2\text{Zr}_2\text{O}_7$  and (\*)  $\text{LiLa}_2\text{NbO}_6$  (pyrochlore).

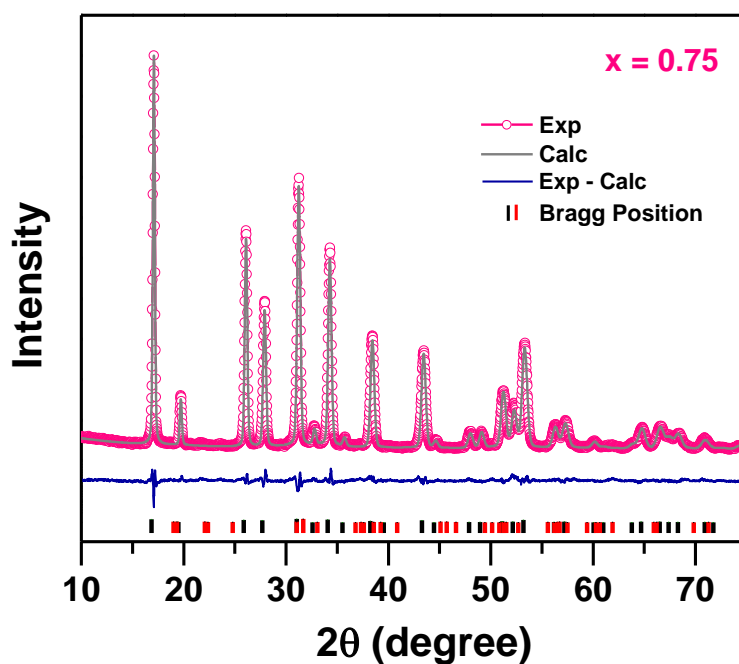
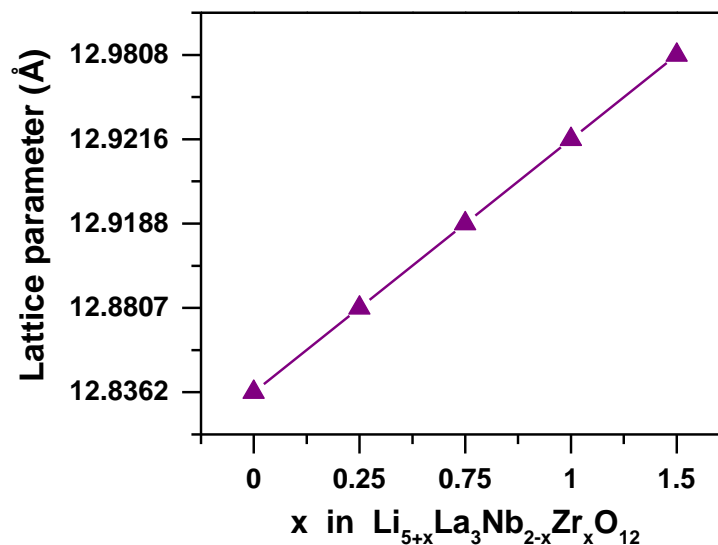


Figure 3. Rietveld refinement of the XRD pattern of LLNZ0.75 powders. The differences between experimental (Exp) and calculated (Calc) data are shown beneath the diagram. Vertical lines indicate the Bragg reflection positions of Garnet structure (black) ICSD #171171 and (red) ICSD #230281.

**Table 2.** Weighted profile  $R$ -factors ( $R_{wp}$  and  $R_p$ ), lattice parameter ( $a$ ), and theoretical density ( $\rho$ ) values determined from the Rietveld refinement for LLNZ synthesized powders as a function of Zr content ( $x$ ).

| $x$  | $R_{wp}$ | $R_p$ | $a$ (Å)     | $\rho$ (g/cm <sup>3</sup> ) |
|------|----------|-------|-------------|-----------------------------|
| 0    | 9.18     | 6.75  | 12.8362(2)  | 5.208                       |
| 0.25 | 11.8     | 8.83  | 12.8807(5)  | 5.152                       |
| 0.75 | 4.92     | 3.81  | 12.91889(4) | 5.101                       |
| 1    | 8.82     | 6.63  | 12.9216(3)  | 5.095                       |
| 1.5  | 8.46     | 6.70  | 12.9808(3)  | 5.020                       |



**Figure 4.** Lattice parameter of Garnet LLNZ solid solutions as a function of Zr content.

Microstructural characterization reveals micron-sized rounded particles, as can be evidenced by SEM micrographs in Figure 5. Elemental mapping analysis of La, Nb, and Zr performed by EDS is presented in pink (Figure 5b), blue (Figure 5c), and orange (Figure 5d) colors, respectively. The elemental mapping evidenced a high degree of distribution and uniformity throughout the sample where no cation segregation has been observed. Since all compositions show similar morphology and elemental homogeneity, we are reporting a representative micrograph of LLNZ0.75. In addition, the experimental compositions are close to the theoretical values for all LLNZ synthesized samples. For example, experimental values were found to be  $\approx 56\%$  (La),  $\approx 24\%$  (Nb), and  $\approx 18\%$  (Zr) for LLNZ0.75 where the expected atomic percentages are 60% (La), 25% (Nb), and 15% (Zr). Small variations are expected since EDS is a semiquantitative analysis.

The junction between particles (Figure 5a) indicates that the intermediate stage of the sintering process has been initiated [37]. Although it might be a detrimental factor for sintering, the combination of high heating rate, caused by the electric current pulses, and pressure application of the SPS system promoted a high degree of densification ( $\geq 96\%$ ), as reported in Table 3, and can be observed in Figure 6. Microstructural evaluation of the dense pellets confirms the high degree of density. A bimodal distribution was identified with grains of approximately 2  $\mu\text{m}$  and submicron-sized grains. The average grain size determined for LLNZ0.75 was in the order of  $1.2 \pm 0.1 \mu\text{m}$ .

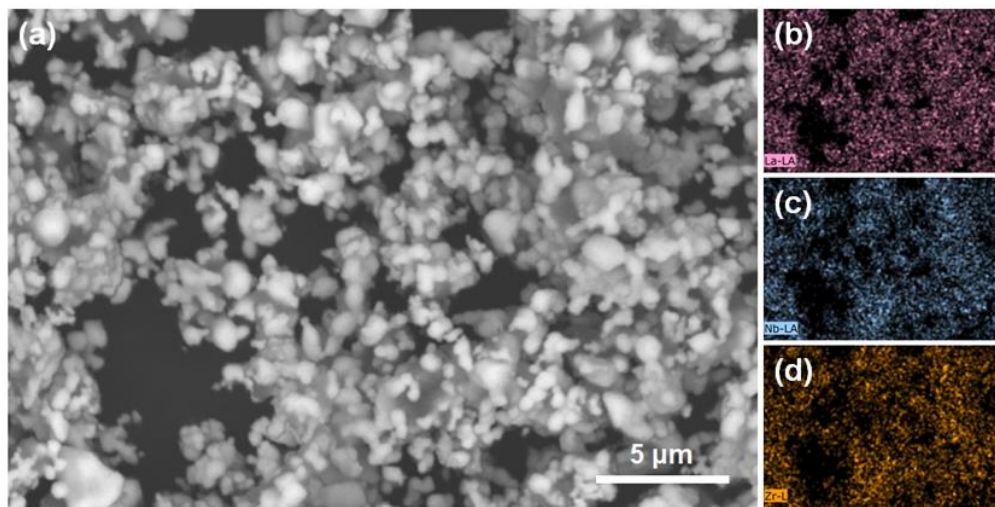


**Figure 5.** SEM image and EDS mapping of LLNZ0.75. (a) SEM micrograph; (b) La, (c) Nb, and (d) Zr mapping.

**Table 3.** Relative density ( $\rho_R$ ), total conductivity ( $\sigma$ ) at 25 °C, and activation energy ( $E_a$ ) for each  $\text{Li}_{5+x}\text{La}_3(\text{Nb}_{2-x}\text{Zr}_x)\text{O}_{12}$  (LLNZ) Garnet sintered pellet.

| $x$  | $\rho_R$ (%) | $\sigma_{25\text{ °C}}$ ( $\text{S}\cdot\text{cm}^{-1}$ ) | $E_a$ (eV)      |
|------|--------------|---|-----------------|
| 0    | 99           | $3.6 \times 10^{-5}$                                      | $0.51 \pm 0.01$ |
| 0.25 | 98           | $3.2 \times 10^{-5}$                                      | $0.49 \pm 0.02$ |
| 0.75 | 98           | $1.3 \times 10^{-4}$                                      | $0.40 \pm 0.02$ |
| 1    | 98           | $1.9 \times 10^{-4}$                                      | $0.38 \pm 0.01$ |

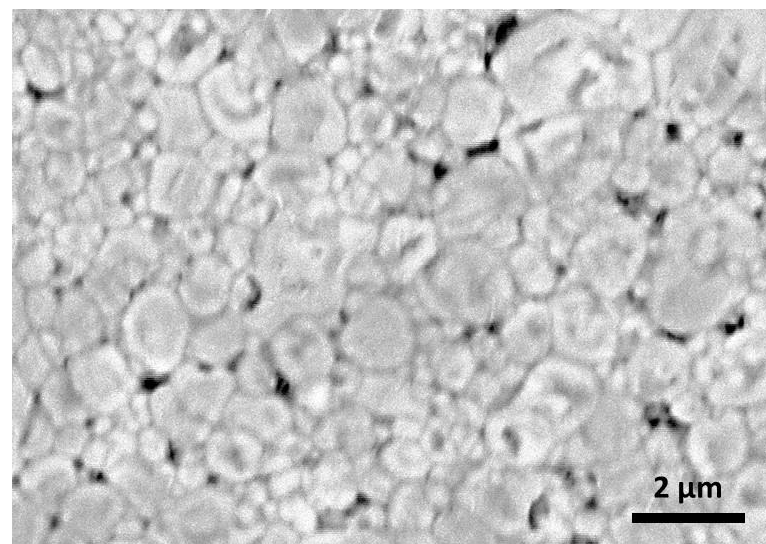


**Figure 6.** SEM micrograph of polished surface of the LLNZ0.75 sintered pellet after heat treatment at 850 °C for 1 h.

XRD patterns of the sintered pellets for the investigated samples are presented in Figure 7. After sintering at 950 °C for 10 min (Figure 7a), only LLNZ0 shows the Garnet structure single phase, while the substitution of  $\text{Zr}^{4+}$  by  $\text{Nb}^{5+}$  ions promoted secondary phases such as  $\text{La}_2\text{Zr}_2\text{O}_7$  and  $\text{LiLa}_2\text{NbO}_6$  (pyrochlore), denoted respectively by (+) and (\*). Formation of the  $\text{La}_2\text{Zr}_2\text{O}_7$  in LLN pellets after SPS was also reported in the literature [20–22,24]. Thus, as an attempt to remove the secondary phases and eliminate residual carbon as well, all samples were conventionally heat treated at 850 °C for 1 h. However,

although conventional heating has eliminated the  $\text{La}_2\text{Zr}_2\text{O}_7$  phase, this process has favored the formation of the pyrochlore structure for LLNZ0.75 and LLNZ1 (Figure 7b). For  $x = 0.75$ , the secondary pyrochlore phase corresponded to 2.9%, determined by the Rietveld method. This may be related to the loss of Li during heat treatment [24,38]. The XRD pattern of the LLNZ0 also showed the pyrochlore diffraction peak after treatment (Figure 7b). Both secondary phases remained in the LLNZ0.25 dense pellets. For  $x < 1.5$ , no significant changes in the lattice parameters of the Garnet structure were detected after sintering at 950 °C for 10 min and heat treatment at 850 °C for 1 h.

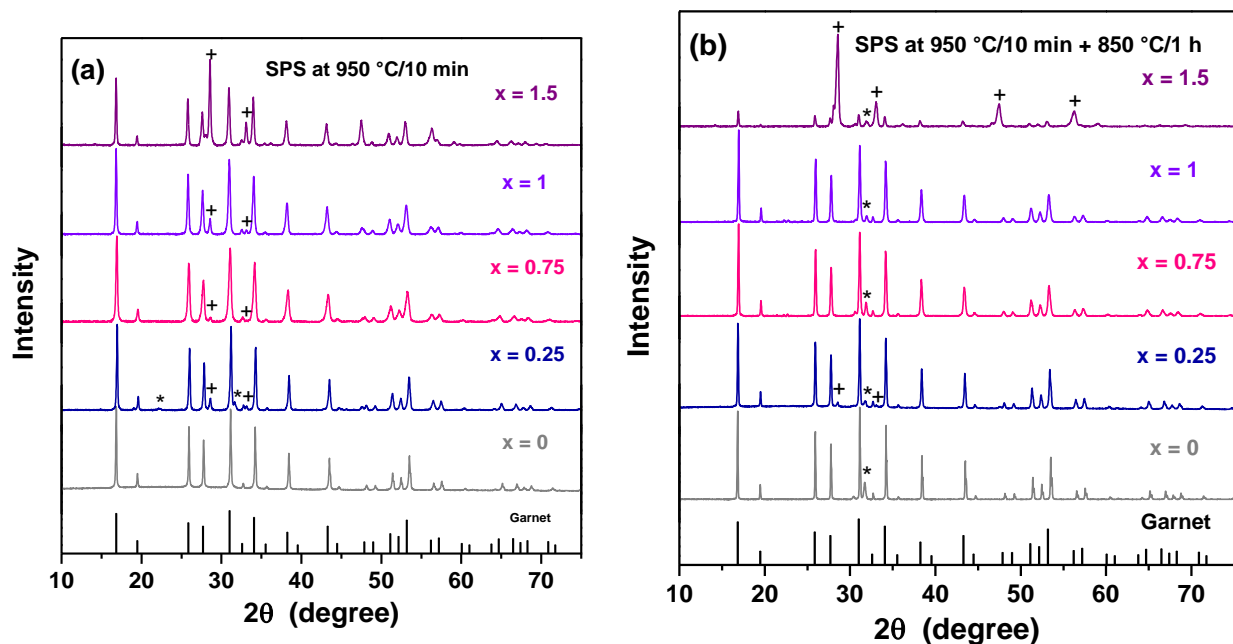


**Figure 7.** X-ray diffraction patterns of LLNZ pellets (a) sintered at 950 °C for 10 min and (b) followed by heat treatment at 850 °C for 1 h. (+)  $\text{La}_2\text{Zr}_2\text{O}_7$  and (\*)  $\text{LiLa}_2\text{NbO}_6$  (pyrochlore).

Samples submitted to the heat treatment at 850 °C for 1 h were selected for electrical measurements except LLNZ1.5 due to the high-intensity peaks characteristic of the pyrochlore phase. Experimental impedance spectroscopy diagrams obtained at 25 °C and the equivalent electrical circuit and equations are reported in Figure 8. In a typical diagram, the opposite of the imaginary part ( $-Z''$ ) is plotted against the real part ( $Z'$ ) of the impedance, giving rise to semicircles that might be associated with electrochemical properties. Both axes were normalized by the sample dimensions area over thickness ( $S/l$ ) and conductivity was determined by fitting of the experimental dataset. The semicircle at high frequencies corresponds to the total lithium-ion electrical conductivity, while the spike observed for all measurements within the low frequency range is attributed to the Au ion-blocking electrode effect. This effect can be verified in the plot of Figure S1, which shows the full frequency range investigated. The equivalent electrical circuit and equations used to extract the ion conductivity [19,24,27] are reported in Figure S1. Clear separation of the grain and grain boundary electrical response was absent for all investigated samples, which agrees with reports in the literature for dense sintered pellets [21]. In addition, any contribution of the secondary phases was identified in the diagrams, indicating that the electrical behavior of the LLNZ has not been affected by the minor amount of the  $\text{La}_2\text{Zr}_2\text{O}_7$  or pyrochlore phase. Interestingly, although LLNZ0 shows a secondary phase after the heat treatment (Figure 7b), no effect of this phase was identified in the electrical measurements (Figure S2).

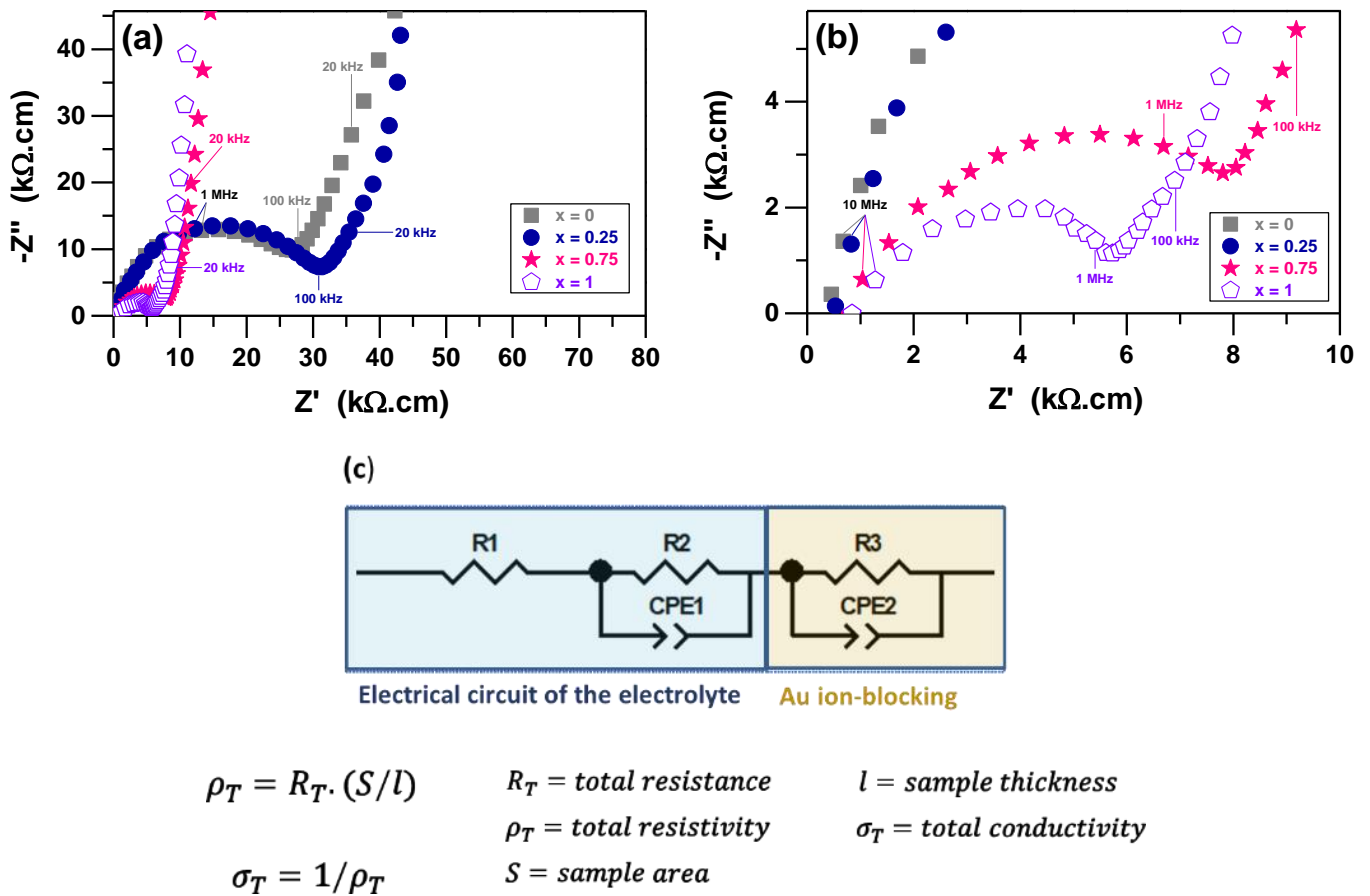


**Figure 8.** Impedance diagrams at 25 °C of the sintered LLNZ Garnet-structured pellets. (a) Limited scale highlighting the semicircles and (b) expanded view of the high-frequency range. (c) The equivalent electrical circuit and equations used to determine lithium-ion conductivity.

It is evident from the impedance diagrams (Figure 8) and Arrhenius plot (Figure 9) that the lithium-ion conductivity of LLNZ0.75 and LLNZ1 are higher than the LLNZ0 and LLNZ0.25 pellets where the values determined at room temperature are summarized in Table 3. At 25 °C, LLNZ0 dense samples exhibit total conductivity of  $3.6 \times 10^{-5} \text{ S.cm}^{-1}$ , which is the same order of magnitude reported previously for LLN produced by solid-state reaction and one order superior to that synthesized by wet chemical methods [11,13,20,27]. The conductivity was increased to  $10^{-4} \text{ S.cm}^{-1}$  by increasing Zr content ( $x \geq 0.75$ ) and reached a maximum value of  $1.9 \times 10^{-4} \text{ S.cm}^{-1}$  for LLNZ1 at 25 °C. A significant decrease of activation energy determined by the Arrhenius plot was observed (Table 3). The activation energy drops from 0.51 eV for  $x = 0$  to 0.38 eV for  $x = 1$ . Thus, the conductivity data show that the increased Zr content significantly increases ionic conductivity by lowering the activation energy, which is in agreement with the trend reported in the literature for Nb-doped LLZ [14]. In addition, similar behavior was reported for Ce-doped LLN, where the lower activation energy was 0.35 eV with maximum lithium-ion conductivity of  $1.4 \times 10^{-4} \text{ S.cm}^{-1}$  for  $\text{Li}_{5.75}\text{La}_3(\text{Nb}_{1.25}\text{Ce}_{0.75})\text{O}_{12}$  at 25 °C [13].

Although the composition range investigated in the current work has been poorly studied in the literature, it is well known that the lithium-ion conductivity is strongly dependent on the lattice parameter in Garnet-like structured ceramics [10,13,14]. The first investigations in the Nb-doped LLZ solid solutions show an increase in ionic conductivity by increasing the Zr/Nb ratio. However, within the Zr-rich limits ( $x > 1.7$ ), an inversion of this trend takes place indicating changes in the ionic conduction mechanism [14]. The ionic conductivity effect evidenced in this work might be explained based on the bottleneck size, which is the main lithium-ion pathway [10,39]. Thus, it has been demonstrated that tailoring

the bottleneck, which is surrounded by  $\text{Nb}^{5+}$  octahedrons and  $\text{La}^{3+}$  decahedrons, can facilitate or hinder lithium-ion diffusivity by increasing or decreasing the lattice parameter reflecting on changes of the crystal lattice symmetry [39]. Therefore, since the ionic radius of  $\text{Zr}^{4+}$  (0.72 Å) [36] is bigger than  $\text{Nb}^{5+}$  (0.64 Å) [36], the increasing Zr/Nb ratio causes crystal lattice distortion by increasing the lattice parameter, as evidenced in Figure 4, increasing the bottleneck size. As a result, it facilitates lithium-ion conduction.

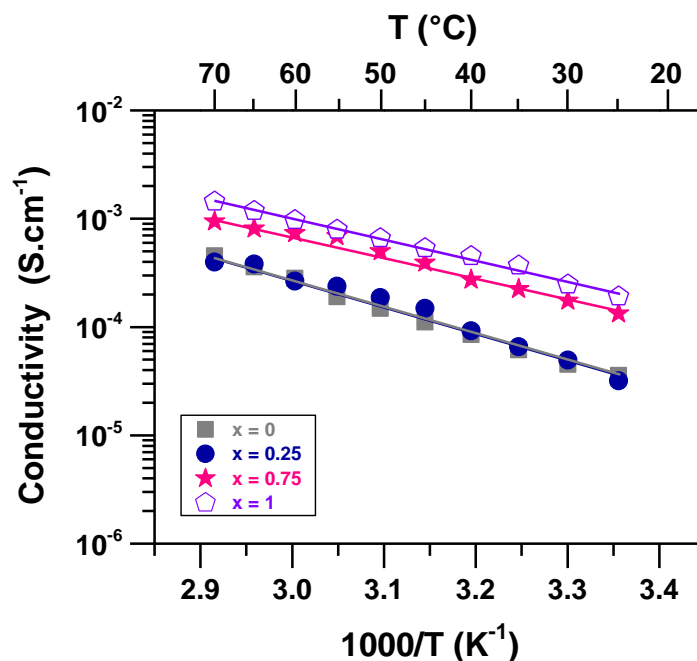


Figure 9. Arrhenius plot of electrical conductivity of the LLNZ sintered dense pellets.

#### 4. Conclusions

Cubic Garnet-type structured Zr-doped  $\text{Li}_5\text{La}_3\text{Nb}_2\text{O}_{12}$  ( $\text{Li}_{5+x}\text{La}_3(\text{Nb}_{2-x}\text{Zr}_x)\text{O}_{12}$ , with  $x$  between 0 and 1.5) solid solutions with high chemical homogeneity were successfully synthesized by solid-state reaction. High relative density (>96%) was achieved by the SPS technique at 950 °C for 10 min for all sintered samples confirmed by SEM micrographs. The elimination of residual  $\text{La}_2\text{Zr}_2\text{O}_7$  was attained by conventional heat treatment at 850 °C for 1 h in Zr-doped samples. High lithium-ion conductivity values of  $1.3 \times 10^{-4}$  and  $1.9 \times 10^{-4} \text{ S.cm}^{-1}$  were obtained for  $x = 0.75$  and 1, respectively, at 25 °C. The activation energy dropped from 0.51 eV for  $x = 0$  to 0.38 eV for  $x = 1$ , indicating that an increased Zr content significantly increased lithium-ion conductivity by lowering the activation energy. The results indicated that the process developed in this study allows production of Garnet-type oxides with high ionic conductivity, even lowering the concentration of the  $\text{Zr}^{4+}$  ions compared with most oxide solid electrolytes reported in the literature without harming its performance. Therefore, the results indicate that Zr-doped  $\text{Li}_5\text{La}_3\text{Nb}_2\text{O}_{12}$  compounds are potential candidates for solid electrolyte application in all-solid-state batteries.

**Supplementary Materials:** The following supporting information can be downloaded at: <https://www.mdpi.com/article/10.3390/batteries9020137/s1>, Figure S1: Impedance diagram of the sintered LLNZ0.75 Garnet-structured pellet obtained at 25 °C within the frequency range of 1 kHz to 13 MHz. Figure S2: Arrhenius plot of the electrical conductivity of LLNZ0 samples sintered by SPS at 950 °C for 10 min before and after conventional heat treatment at 850 °C for 1 h, which promoted pyrochlore phase formation, as evidenced by the X-ray diffraction patterns in Figure 6.

**Author Contributions:** Conceptualization, C.G., R.M., L.P. and M.B.; formal analysis, S.R. and R.G.; investigation and methodology, S.R., R.G., J.K., M.F., F.O., A.S. and C.G.; project administration, C.G., R.M., L.P., H.F. and M.B.; supervision, C.G., H.F. and M.B.; writing—review and editing, S.R., R.G., J.K. and C.G. All authors have read and agreed to the published version of the manuscript.

**Funding:** This work was financially supported by Companhia Brasileira de Metalurgia e Mineração (CBMM) and Empresa Brasileira de Pesquisa e Inovação Industrial (EMBRAPPII, grant number Pele #2005-0008).

**Data Availability Statement:** Not applicable.

**Acknowledgments:** The authors acknowledge Cassio Morilla dos Santos for the Rietveld refinement assistance.

**Conflicts of Interest:** The authors declare no conflict of interest.

## References

1. Liang, Y.; Zhao, C.; Yuan, H.; Chen, Y.; Zhang, W.; Huang, J.; Yu, D.; Liu, Y.; Titirici, M.; Chueh, Y.; et al. A Review of rechargeable batteries for portable electronic devices. *InfoMat* **2019**, *1*, 6–32. [\[CrossRef\]](#)
2. Xie, J.; Lu, Y.-C. A retrospective on lithium-ion batteries. *Nat. Commun.* **2020**, *11*, 2499. [\[CrossRef\]](#) [\[PubMed\]](#)
3. Masias, A.; Marcicki, J.; Paxton, W.A. Opportunities and challenges of lithium ion batteries in automotive applications. *ACS Energy Lett.* **2021**, *6*, 621–630. [\[CrossRef\]](#)
4. Sun, P.; Bisschop, R.; Niu, H.; Huang, X. A Review of battery fires in electric vehicles. *Fire Technol.* **2020**, *56*, 1361–1410. [\[CrossRef\]](#)
5. Feng, X.; Ouyang, M.; Liu, X.; Lu, L.; Xia, Y.; He, X. Thermal runaway mechanism of lithium ion battery for electric vehicles: A review. *Energy Storage Mater.* **2018**, *10*, 246–267. [\[CrossRef\]](#)
6. Champion, C.L.; Li, W.; Lucht, B.L. Thermal decomposition of LiPF<sub>6</sub>-based electrolytes for lithium-ion batteries. *J. Electrochem. Soc.* **2005**, *152*, A2327. [\[CrossRef\]](#)
7. Chen, Y.; Kang, Y.; Zhao, Y.; Wang, L.; Liu, J.; Li, Y.; Liang, Z.; He, X.; Li, X.; Tavajohi, N.; et al. A review of lithium-ion battery safety concerns: The issues, strategies, and testing standards. *J. Energy Chem.* **2021**, *59*, 83–99. [\[CrossRef\]](#)
8. Janek, J.; Zeier, W.G. A solid future for battery development. *Nat. Energy* **2016**, *1*, 16141. [\[CrossRef\]](#)
9. Sun, Y.-K. Promising all-solid-state batteries for future electric vehicles. *ACS Energy Lett.* **2020**, *5*, 3221–3223. [\[CrossRef\]](#)
10. Ramakumar, S.; Deviannapoorani, C.; Dhivya, L.; Shankar, L.S.; Murugan, R. Lithium Garnets: Synthesis, structure, Li<sup>+</sup> conductivity, Li<sup>+</sup> dynamics and applications. *Prog. Mater. Sci.* **2017**, *88*, 325–411. [\[CrossRef\]](#)
11. Thangadurai, V.; Kaack, H.; Weppner, W.J.F. Novel fast lithium ion conduction in garnet-type Li<sub>5</sub>La<sub>3</sub>M<sub>2</sub>O<sub>12</sub> (M = Nb, Ta). *J. Am. Ceram. Soc.* **2003**, *86*, 437–440. [\[CrossRef\]](#)
12. Peng, H.; Wu, Q.; Xiao, L. Low temperature synthesis of Li<sub>5</sub>La<sub>3</sub>Nb<sub>2</sub>O<sub>12</sub> with cubic garnet-type structure by sol-gel process. *J. Sol-Gel Sci. Technol.* **2013**, *66*, 175–179. [\[CrossRef\]](#)
13. Dong, B.; Stockham, M.P.; Chater, P.A.; Slater, P.R. X-ray pair distribution function analysis and electrical and electrochemical properties of cerium doped Li<sub>5</sub>La<sub>3</sub>Nb<sub>2</sub>O<sub>12</sub> garnet solid-state electrolyte. *Dalt. Trans.* **2020**, *49*, 11727–11735. [\[CrossRef\]](#)
14. Ohta, S.; Kobayashi, T.; Asaoka, T. High lithium ionic conductivity in the garnet-type oxide Li<sub>7-x</sub>La<sub>3</sub>(Zr<sub>2-x</sub>Nb<sub>x</sub>)O<sub>12</sub> (x = 0–2). *J. Power Sources* **2011**, *196*, 3342–3345. [\[CrossRef\]](#)
15. Murugan, R.; Thangadurai, V.; Weppner, W. Fast lithium ion conduction in garnet-type Li<sub>7</sub>La<sub>3</sub>Zr<sub>2</sub>O<sub>12</sub>. *Angew. Chemie Int. Ed.* **2007**, *46*, 7778–7781. [\[CrossRef\]](#)
16. Wang, C.; Fu, K.; Kammampata, S.P.; McOwen, D.W.; Samson, A.J.; Zhang, L.; Hitz, G.T.; Nolan, A.M.; Wachsmann, E.D.; Mo, Y.; et al. Garnet-type solid-state electrolytes: Materials, interfaces, and batteries. *Chem. Rev.* **2020**, *120*, 4257–4300. [\[CrossRef\]](#)
17. Teng, S.; Wang, W.; Tiwari, A. Novel low temperature molten salt synthesis of a Li<sub>5</sub>La<sub>3</sub>Nb<sub>2</sub>O<sub>12</sub> solid state electrolyte and its properties. *MRS Proc.* **2014**, *1679*, 7–11. [\[CrossRef\]](#)
18. Thangadurai, V.; Weppner, W. Li<sub>6</sub>Ala<sub>2</sub>Nb<sub>2</sub>O<sub>12</sub> (A = Ca, Sr, Ba): A new class of fast lithium ion conductors with garnet-like structure. *J. Am. Ceram. Soc.* **2005**, *88*, 411–418. [\[CrossRef\]](#)
19. Truong, L.; Thangadurai, V. Soft-chemistry of garnet-type Li<sub>5+x</sub>Ba<sub>x</sub>La<sub>3-x</sub>Nb<sub>2</sub>O<sub>12</sub> (x = 0, 0.5, 1): Reversible H<sup>+</sup> ↔ Li<sup>+</sup> ion-exchange reaction and their X-ray, <sup>7</sup>Li MAS NMR, IR, and AC impedance spectroscopy characterization. *Chem. Mater.* **2011**, *23*, 3970–3977. [\[CrossRef\]](#)
20. Lustosa, G.M.M.M.; Franchetti, M.G.S.; de Souza, A.; Goulart, F.A.B.; da Conceição, L.; Berton, M.A.C. Fast synthesis and sintering of Li<sub>5</sub>La<sub>3</sub>Nb<sub>2</sub>O<sub>12</sub> garnet ceramic. *Mater. Chem. Phys.* **2021**, *257*, 123848. [\[CrossRef\]](#)
21. Ahmad, M.M. Enhanced lithium ionic conductivity and study of the relaxation and giant dielectric properties of spark plasma sintered Li<sub>5</sub>La<sub>3</sub>Nb<sub>2</sub>O<sub>12</sub> nanomaterials. *Ceram. Int.* **2015**, *41*, 6398–6408. [\[CrossRef\]](#)
22. Baek, S.-W.; Lee, J.-M.; Kim, T.Y.; Song, M.-S.; Park, Y. Garnet related lithium ion conductor processed by spark plasma sintering for all solid state batteries. *J. Power Sources* **2014**, *249*, 197–206. [\[CrossRef\]](#)
23. Ji, Y.; Zhou, C.; Lin, F.; Li, B.; Yang, F.; Zhu, H.; Duan, J.; Chen, Z. Submicron-sized Nb-doped lithium garnet for high ionic conductivity solid electrolyte and performance of quasi-solid-state lithium battery. *Materials* **2020**, *13*, 560. [\[CrossRef\]](#) [\[PubMed\]](#)
24. Yamada, H.; Ito, T.; Hongahally Basappa, R. Sintering mechanisms of high-performance garnet-type solid electrolyte densified by spark plasma sintering. *Electrochim. Acta* **2016**, *222*, 648–656. [\[CrossRef\]](#)
25. Nemori, H.; Matsuda, Y.; Matsui, M.; Yamamoto, O.; Takeda, Y.; Imanishi, N. Relationship between lithium content and ionic conductivity in the Li<sub>5+2x</sub>La<sub>3</sub>Nb<sub>2-x</sub>Sc<sub>x</sub>O<sub>12</sub> system. *Solid State Ion.* **2014**, *266*, 9–12. [\[CrossRef\]](#)

26. Stockham, M.P.; Dong, B.; Ding, Y.; Li, Y.; Slater, P.R. Evaluation of the effect of site substitution of Pr doping in the lithium garnet system  $\text{Li}_5\text{La}_3\text{Nb}_2\text{O}_{12}$ . *Dalt. Trans.* **2020**, *49*, 10349–10359. [[CrossRef](#)]
27. Peng, H.; Feng, L.; Li, L.; Zhang, Y.; Zou, Y. Effect of Ge substitution for Nb on Li ion conductivity of  $\text{Li}_5\text{La}_3\text{Nb}_2\text{O}_{12}$  solid state electrolyte. *Electrochim. Acta* **2017**, *251*, 482–487. [[CrossRef](#)]
28. Peng, H.; Feng, L.; Li, L.; Zhang, Y.; Zou, Y. Synthesis of  $\text{Li}_{5+x}\text{La}_3\text{Hf}_x\text{Nb}_{2-x}\text{O}_{12}$  ( $x = 0.2-1$ ) ceramics with cubic garnet-type structure. *Mater. Lett.* **2017**, *194*, 138–141. [[CrossRef](#)]
29. Pinzaru, D.; Thangadurai, V. Synthesis, structure and Li ion conductivity of garnet-like  $\text{Li}_{5+2x}\text{La}_3\text{Nb}_{2-x}\text{Sm}_x\text{O}_{12}$  ( $0 \leq x \leq 0.7$ ). *J. Electrochem. Soc.* **2014**, *161*, A2060–A2067. [[CrossRef](#)]
30. Kan, W.H.; Truong, L.; Thangadurai, V. Effect of V-doping on the structure and conductivity of garnet-type  $\text{Li}_5\text{La}_3\text{Nb}_2\text{O}_{12}$ . *Ionics* **2015**, *21*, 373–379. [[CrossRef](#)]
31. Narayanan, S.; Baral, A.K.; Thangadurai, V. Dielectric characteristics of fast Li ion conducting garnet-type  $\text{Li}_{5+2x}\text{La}_3\text{Nb}_{2x}\text{Y}_x\text{O}_{12}$  ( $x = 0.25, 0.5$  and  $0.75$ ). *Phys. Chem. Chem. Phys.* **2016**, *18*, 15418–15426. [[CrossRef](#)] [[PubMed](#)]
32. Imagawa, H.; Ohta, S.; Kihira, Y.; Asaoka, T. Garnet-type  $\text{Li}_{6.75}\text{La}_3\text{Zr}_{1.75}\text{Nb}_{0.25}\text{O}_{12}$  synthesized by coprecipitation method and its lithium ion conductivity. *Solid State Ion.* **2014**, *262*, 609–612. [[CrossRef](#)]
33. Munir, Z.A.; Anselmi-Tamburini, U.; Ohyanagi, M. The effect of electric field and pressure on the synthesis and consolidation of materials: A review of the spark plasma sintering method. *J. Mater. Sci.* **2006**, *41*, 763–777. [[CrossRef](#)]
34. Momma, K.; Izumi, F. VESTA 3 for three-dimensional visualization of crystal, volumetric and morphology data. *J. Appl. Crystallogr.* **2011**, *44*, 1272–1276. [[CrossRef](#)]
35. Cussen, E.J. The structure of lithium garnets: Cation disorder and clustering in a new family of fast  $\text{Li}^+$  conductors. *Chem. Commun.* **2006**, *4*, 412–413. [[CrossRef](#)]
36. Shannon, R.D. Revised effective ionic radii and systematic studies of interatomic distances in halides and chalcogenides. *Acta Crystallogr. Sect. A* **1976**, *32*, 751–767. [[CrossRef](#)]
37. German, R.M. *Sintering: From Empirical Observations to Scientific Principles*, 1st ed.; Elsevier: Woburn, MA, USA, 2014; ISBN 9780124016828.
38. Paolella, A.; Zhu, W.; Bertoni, G.; Savoie, S.; Feng, Z.; Demers, H.; Garipey, V.; Girard, G.; Rivard, E.; Delaporte, N.; et al. Discovering the influence of lithium loss on garnet  $\text{Li}_7\text{La}_3\text{Zr}_2\text{O}_{12}$  electrolyte phase stability. *ACS Appl. Energy Mater.* **2020**, *3*, 3415–3424. [[CrossRef](#)]
39. Chen, F.; Xu, L.; Li, J.; Yang, Y.; Shen, Q. Effect of bottleneck size on lithium migration in lithium garnets  $\text{Li}_7\text{La}_3\text{Zr}_2\text{O}_{12}$  (LLZO). *Ionics* **2020**, *26*, 3193–3198. [[CrossRef](#)]

**Disclaimer/Publisher's Note:** The statements, opinions and data contained in all publications are solely those of the individual author(s) and contributor(s) and not of MDPI and/or the editor(s). MDPI and/or the editor(s) disclaim responsibility for any injury to people or property resulting from any ideas, methods, instructions or products referred to in the content.